

Bottom and top reconstruction as benchmarks for the ILD Detector

M.S. Amjad^a, A. Irlles^b, V. Lohezic^c, Y. Okugawa^d, R. Pöschl^b, F. Richard^b,
H. Yamamoto^d, R. Yonamine^d

^aNational University of Technology, Islamabad, Pakistan

^bLaboratoire de l'Accélérateur Linéaire, CNRS/IN2P3 et Université de Paris-Sud, Centre Scientifique d'Orsay
Bâtiment 200, BP 34, 91898 Orsay CEDEX, France

^cUniversité Paris-Sud, 15 Rue Georges Clemenceau, 91400 Orsay, France

^dTohoku University, 6-3 Aoba Aramaki-aza Aoba-ku, Sendai 980-8578, Japan

Abstract

A comprehensive study of bottom-quark pair and top-quark pair production using the semi-leptonic decay channel at $\sqrt{s} = 500$ GeV is presented that benchmark the performance of the current so-called *large* and *small* models of the ILD Detector. The event reconstruction exploits distinguished features of the detector such as lepton identification, vertex charge reconstruction and particle ID with the central TPC of the ILD Detector. With these techniques the final state leptons, the b -quark and \bar{b} -quark and the W can be unambiguously reconstructed. Both detector models perform similarly well with a slight advantage of the large detector model. In case of top quark pair production the selection efficiency is between 30% and 60% for semi-leptonic events. For this channel the note presents an update of the perspective of the physics potential w.r.t. earlier studies for an integrated luminosity of 3200 fb^{-1} . The results for $e^+e^- \rightarrow b\bar{b}$ demonstrate that also this channel can accurately measured at $\sqrt{s} = 500$ GeV.

1. Introduction

Heavy quarks may be messengers of new physics of primary importance [1]. Their large mass compared with other fermions can be explained in Randall Sundrum models [2, 3] featuring warped extra dimensions that are dual to model, which assume that the heavy quarks are composite objects [4]. High precision e^+e^- collisions with polarised beams around the TeV scale are ideally suited to detect new physics effects [5, 6]. Precise measurements of the electroweak couplings of third-generation quarks require superb detector performance in terms of flavour tagging including the event by event determination of the charge of the final state jets to avoid for example migrations in polar angle spectra and/or to reconstruct events in which the heavy quark charge is the only handle to distinguish between particles and anti-particles. The charge determination happens mainly by a combination of the determination of the summed charge of tracks pointing to a secondary vertex or by the identification of the charge of a final state Kaon. This in turn requires a successful particle identification by the detector. Therefore processes with heavy quark final states, i.e. $e^+e^- \rightarrow \phi b\bar{b}$ and $e^+e^- \rightarrow t\bar{t}$ are highly relevant for the benchmarking of the detector performance. In short one can test the following detector capacities.

- Track finding efficiency
- Stringent test of (secondary) vertexing
- Particle ID

In case of $e^+e^- \rightarrow t\bar{t}$ leptonic and semi-leptonic decays of the t -quark pair provide an important additional handle for the accurate measurement of the final state. The analysis presented in this

41 note focuses on the semi-leptonic decay mode of the top-quark pair. The analysis of $t\bar{t}$ production
 42 and $b\bar{b}$ production share a number of commonalities. Therefore these two analyses are joined in this
 43 note. The analyses presented in this note start out from the PhD thesis of Sviatoslav Bilokin that are
 44 based on the DBD samples and software versions [7]. This work has in part been published in Ref [6].
 45 The analyses are ported to the large, IDR-L, and small, IDR-S, detector models, respectively, of the
 46 ILD detector [8] for the International Linear Collider [9]. The research program includes high-statistics
 47 running at $\sqrt{s} = 250$ GeV and $\sqrt{s} = 500$ GeV. For further details of the operation scenarios see Ref. [10].
 48 For the process $e^+e^- \rightarrow b\bar{b}$ an analysis at $\sqrt{s} = 500$ GeV is presented instead of $\sqrt{s} = 250$ GeV as
 49 in Ref. [6]. The results here benefit from a refined analysis strategy for the ILD paper that is under
 50 review in ILD.

51 2. Methods, tools and Monte Carlo samples

52 For the event reconstruction we use the `ILCSOFT` version `v02-00-02`. The software allows for a full
 53 detector simulation and event reconstruction including digitisation steps. For the analyses presented
 54 we use the versions `ILD_s5_o1_v02` and `ILD_15_o1_v02` of the detector model.

55 For the event reconstruction we use the following methods

- 56 • ‘Core tools’

- 57 – In case of $e^+e^- \rightarrow t\bar{t}$ we use the standard Durham algorithm for jet clustering and the
 58 Valencia algorithm for $\gamma\gamma$ background removal.

- 59 – In case of $e^+e^- \rightarrow b\bar{b}$ we use the Valencia jet algorithm implemented in the `LCFIPlus`
 60 package [11] as available in `ILCSOFT`. We apply the option in which the algorithm does not
 61 break secondary vertices. In this algorithm the distance between two objects is calculated
 62 as

$$d_{ij} = 2 \min(E_i^{2\beta}, E_j^{2\beta})(1 - \cos \theta_{ij})/R^2 \quad (1)$$

63 The distance of a particle i to the beam is calculated according to.

$$d_{iB} = E^{2\beta} \sin^{2\gamma} \theta_{iB} \quad (2)$$

64 The jet algorithm is run with the following settings: $\alpha = \beta = \gamma = 1$, $R = 1.4$

- 65 – We use the standard `LeptonFinder` of ILD to identify isolated electrons and muons in semi-
 66 leptonic $t\bar{t}$ events.

- 67 • Tools developed for the study

- 68 – We identify reconstructed tracks that have not been associated to secondary vertices from
 69 B-Meson decays but belongs to this decay according to the Monte Carlo Truth information.
 70 It then recovers the ‘lost’ tracks by means of the impact parameters d_0 (transversal) and z_0
 71 (longitudinal). In this present note the recovery uses only the impact parameter d_0 since
 72 the algorithms needs to be adapted for the vertex smearing present in the simulation for
 73 the IDR.

- 74 – We identify Kaons by means of the dE/dx measured in the TPC of ILD. It selects a strip in
 75 the dE/dx -momentum plane with a high kaon concentration. The efficiency and the purity
 76 of the Kaon selection vary as a function of the width of this strip.

- 77 – We finally calculate the jet charge and the polar angle of the bottom and top quark pair,
 78 respectively.

- 79 • The following method combines the results of the two (nearly independent) charge measurements
 80 on the b and \bar{b} jet into a robust charge determination.

$$\left. \begin{aligned} N_{acc} &= Np^2 + Nq^2 \\ N_{rej} &= 2Npq \\ 1 &= p + q \end{aligned} \right\} N_{corr} = N_{acc} \cdot \frac{p^2}{p^2 + q^2} \quad (3)$$

81 where N is total number of events, N_{acc} and N_{rej} are the number of events that were accepted
 82 and rejected, respectively. The p and q values represent the probabilities for a correct or an
 83 incorrect reconstruction of the b -quark charge, respectively. Solving this equation allows to
 84 correct for migrations caused by imperfect reconstruction or $B^0 - \bar{B}^0$ oscillations in the resulting
 85 polar angle spectrum. The correction has been applied to the $b\bar{b}$ studies but not (yet) for $t\bar{t}$.
 86 For the latter the selection scheme in $t\bar{t}$ is more involved rendering its application less straight
 87 forward since e.g. the b -quarks are not necessarily back-to-back.

88 2.1. Monte Carlo samples

89 Samples generated with WHIZARD 1.95. Top quark pair production is the dominant process in
 90 the $e^+e^- \rightarrow b\bar{b}\ell\nu q\bar{q}$ sample, but it contains also single t and WWZ . In case of the t quark study
 91 we have analysed samples for the beam polarisations $\mathcal{P}_{e^-}, \mathcal{P}_{e^+} = \pm 1, \mp 1$. In total we analyse about
 92 2200 fb^{-1} for each of the beam polarisations but we discard final states for which $W \rightarrow \tau\nu$. In case
 93 of the b quark study we have studied only the configuration $\mathcal{P}_{e^-}, \mathcal{P}_{e^+} = \mp 1$ since this study is just
 94 considered as a supporting study for the t quark analysis and the chosen polarisation configuration is
 95 the more challenging for the detector performance due to larger migration effects in the polar angle
 96 reconstruction. $e^+e^- \rightarrow b\bar{b}$: The $b\bar{b}$ events are extracted from a sample of simulated $q\bar{q}$. The total
 97 integrated luminosity is about 46 fb^{-1} . The genuine $e^+e^- \rightarrow b\bar{b}$ at 500 GeV is about 4% of the total
 98 cross section.

99 Note that the analysis of the $e_R^+e_L^- \rightarrow t\bar{t}$ came quite late in the study since it is generally considered
 100 that the $e_L^+e_R^- \rightarrow t\bar{t}$ is the more challenging channel. Therefore, the corresponding control plots in
 101 Secs. 3 and 4.2 are only given for the latter in this note.

102 3. Efficiencies and Control plots

103 Figure 1 demonstrates that the studies presented in this note test the detector performance for
 104 very different momenta of the final state b quark.

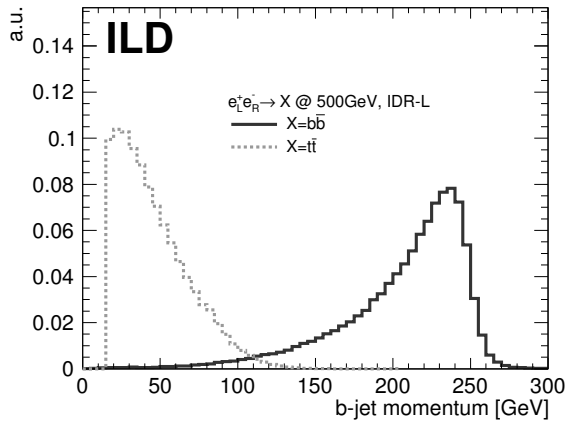


Figure 1: Momentum of the b -jet with cheated identification for $e^+e^- \rightarrow b\bar{b}$ and $e^+e^- \rightarrow t\bar{t}$ processes.

105 The Figs. 2 and 3 show the missed tracks before and after vertex recovery for the $e^+e^- \rightarrow b\bar{b}$ and
 106 $e^+e^- \rightarrow t\bar{t}$ analyses, respectively. Both figures suggest a systematic improvement in the assignment of
 107 secondary vertices.

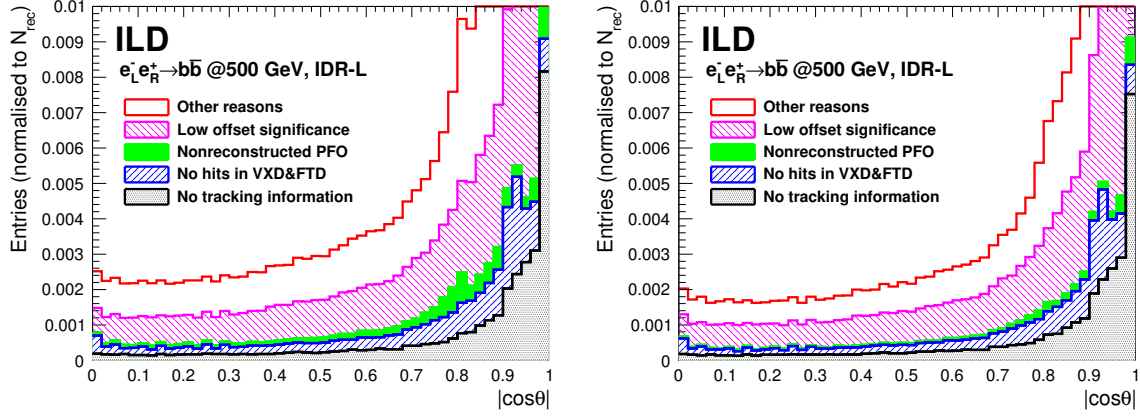


Figure 2: Polar angle of missed tracks before (left) and after (right) vertex recovery in case of the $e^+e^- \rightarrow b\bar{b}$ process.

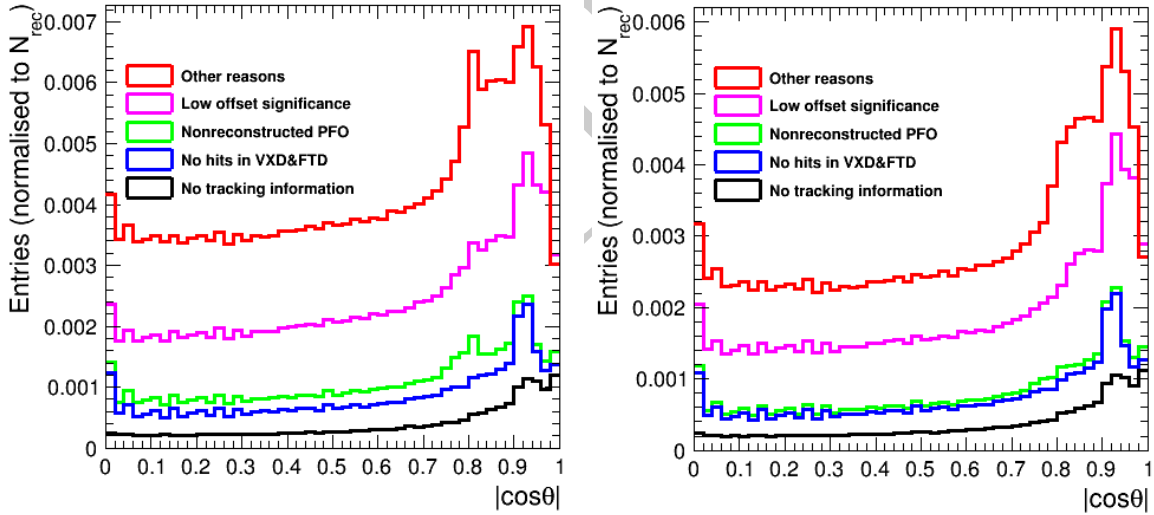


Figure 3: Polar angle of missed tracks before (left) and after (right) vertex recovery in case of the $e^+e^- \rightarrow t\bar{t}$ process.

108 This improvement is quantified in Figs. 4 and 5 where the purity of the b -charge reconstruction
 109 is shown as a function of the b -tag value, the reconstructed b -momentum $|p_{had}|$ the number of
 110 reconstructed tracks assigned to a secondary vertex N_{rec} and finally the polar angle of the b -hadron.
 111 here denoted as $|\cos \theta|$. The b -charge purity is defined as

$$p_b = N_{correct}/N_{jet,tot}. \quad (4)$$

112 with $N_{correct}$ being the number of b -jets with correctly reconstructed b quark charge. This value nor-
 113 malised to the total number of b -jets $N_{b-jet,tot}$. for which a charge assignment according to e.g. Table 2
 114 can be made.

115 The improvement is larger for the process $e^+e^- \rightarrow t\bar{t}$ than for $e^+e^- \rightarrow b\bar{b}$. Qualitatively this is
 116 expected since as a consequence of the different b -jet momenta, see Fig. 1, also the tracks produced
 117 in the decay of the b -hadron are softer in case of top-pair production. In case of $e^+e^- \rightarrow t\bar{t}$ the
 118 improvement is 10% over a large range in $|\cos\theta|$ and mainly driven by three to five prong decays.
 119 Both results will further improve once the vertex recovery takes also the the impact parameter z_0 into
 120 account. All results shown so far in this section have been obtained for the large detector model. The
 121 conclusions for the small detector model are similar.

122 The lower right panels of Figs. 4 and 5 show a drop in purity for large values of $|\cos\theta|$. This is
 123 compatible with the drop in acceptance that is shown in Fig. 6 for the case $e^+e^- \rightarrow b\bar{b}$ as a function
 124 of the polar angle of the reconstructed b -jet $|\cos\theta_b|$. Within statistical errors the results are the same
 125 for the large and the small detector model. However, towards large values of $|\cos\theta_b|$ the large detector
 126 performs systematically better than the small detector.

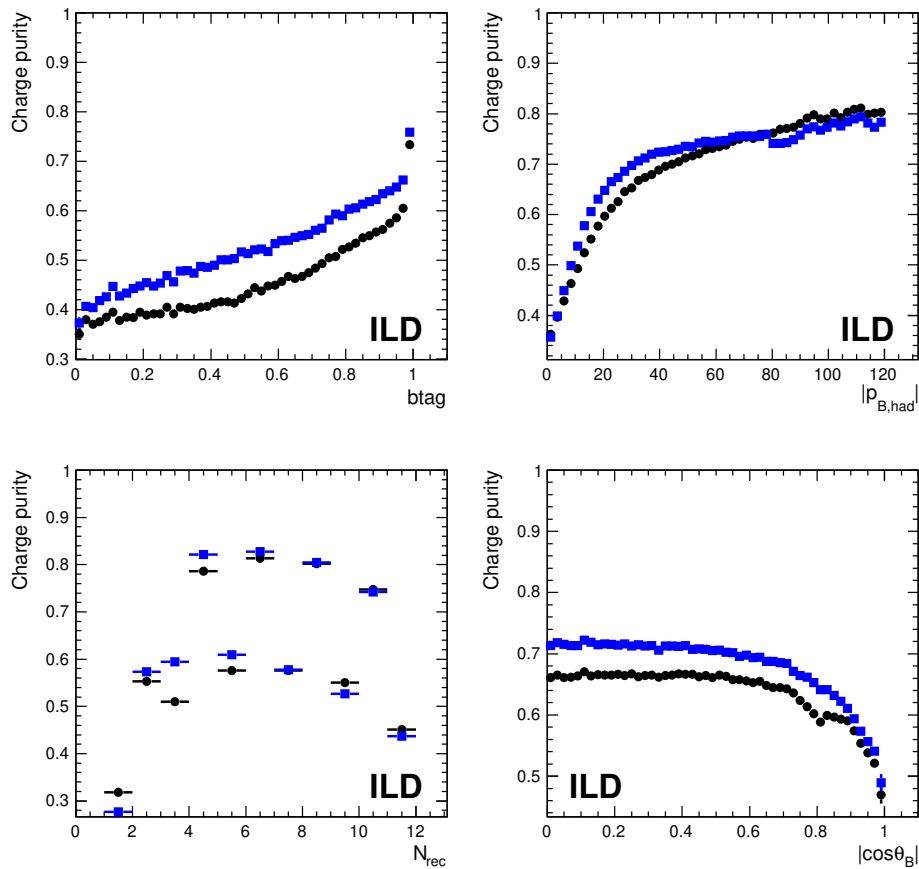


Figure 4: Purity before and after vertex recovery in case of the $e^+e^- \rightarrow t\bar{t}$ process for different observables.

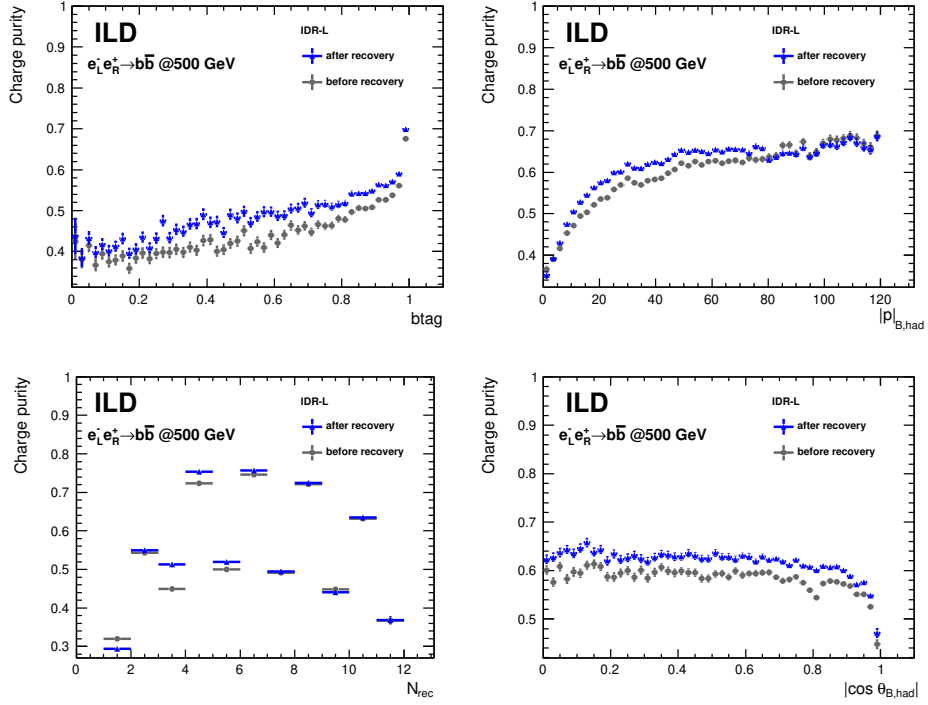


Figure 5: Purity before and after vertex recovery in case of the $e^+e^- \rightarrow t\bar{t}$ process for different observables.

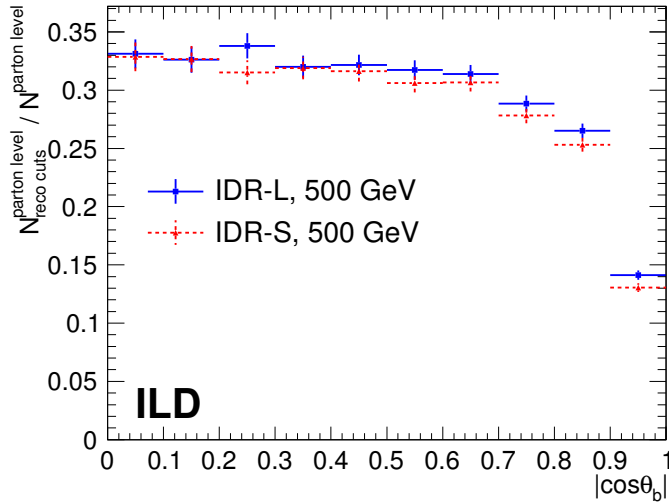


Figure 6: Detector acceptance distribution for b-tagged jets. Note the figure shows the acceptance after the full selection given in Tab. 1.

127 A component that distinguishes the ILD Detector from other proposals for e^+e^- colliders is the TPC
 128 as the central tracking system. Beside the precise momentum measurement the dE/dx measurement
 129 in the gaseous medium allows for a particle identification. Since around 87% of B-Mesons (neutral or
 130 charged) contain a charged Kaon among their decay products the particle ID can support greatly the

131 charge determination of the b quark.

132 The left part of Fig. 7 shows the dE/dx values obtained in simulation for different particle types
 133 as a function of the particle momentum. The lines indicate a strip with an accumulation of signals
 134 produced by Kaons. A minimum momentum of 2 GeV is required for the selection of Kaons. The
 135 right part of Fig. 7 shows the variation of the purity as a function of the Kaon selection efficiency
 136 that corresponds to a variation of the width of the strip in the previous figure. A closer look into the
 137 separation power in different momentum ranges is given in App. A.

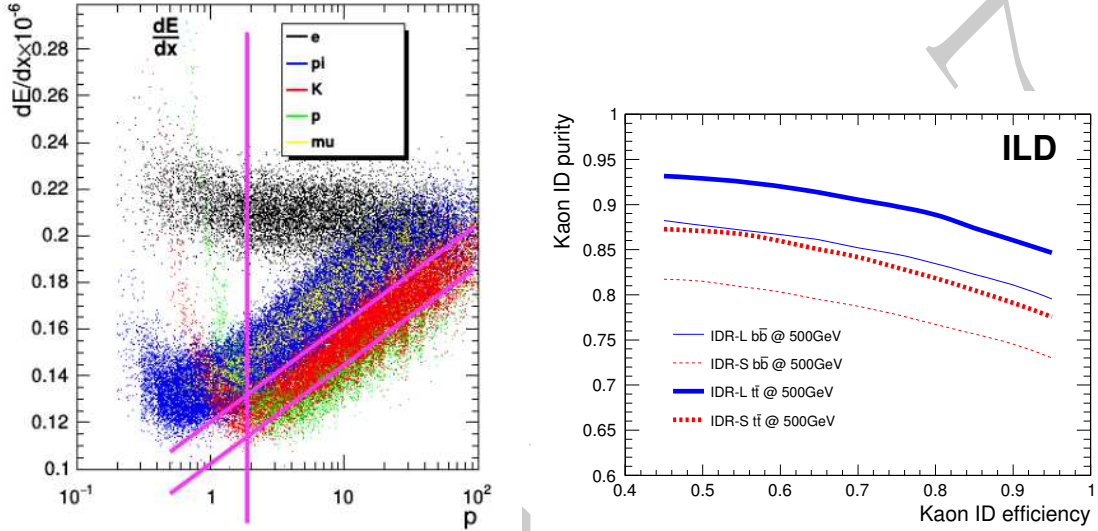


Figure 7: Left: Simulated dE/dx spectrum for different particle types. The lines indicate the cuts for the Kaon selection. Right: Purity of the Kaon selection as a function of the Kaon selection efficiency.

138 4. Event selection

139 In the following the event selection of the two final states under study will be presented. The
 140 different complexities of the final states require different set of cuts. The t quark is composed from its
 141 decay products, the b quark and the W boson and the final state le

142 4.1. Analysis details specific to the $e_L^- e_R^+ \rightarrow b\bar{b}$ analysis

143 Table 1 shows the selection efficiencies for the $e_L^- e_R^+ \rightarrow b\bar{b}$ analysis. In this case events that are
 144 subject to the radiative return to the Z , implying an energetic final state photon, have to be suppressed.
 145 Therefore cuts on the sum of the masses of the two jets and a cut on the photon energy are introduced.
 146 The overall efficiency after selection of events with consistent b quark charge is with around 28% to
 147 29% similar for both detector models. For the b -charge measurement opposite charges in opposite jets
 148 are required. The charges are either derived from the tracks pointing to the secondary vertex or from
 149 the Kaon charge or from a combination of both. An event is selected if there is one combination with
 150 a consistent result. The efficiencies for the different methods are given in Tab. 2. The purity of the
 151 different methods is shown in Fig. 8. In both cases there is no large difference between the two detector
 152 models although the large detector seems to perform slightly better for the double Kaon method. This
 153 suggests that the smaller outer radius of the TPC puts a, however minor, on the dE/dx measurement.

154

$e_L^- e_R^+ \rightarrow b\bar{b}$ at 500 GeV

	IDR-L			IDR-S		
	Signal	B _{q\bar{q}} /S	B _{rad.Z} /S	Signal	B _{q\bar{q}} /S	B _{rad.Z} /S
Full sample	100.0%	1800.5%	359.1%	100.0%	1800.6%	359.0%
$b_{tag}(jet_1) > 0.9$ and $b_{tag}(jet_2) > 0.2$	70.2%	2.3%	147.7%	69.9%	2.3%	149.0%
$m_{jet_1+jet_2} > 200 GeV$	68.2%	1.4%	6.7%	67.8%	1.2%	6.7%
$E_{photon} < 100 GeV$	64.8%	1.3%	1.7%	64.3%	1.2%	1.6%
double jet-charge measurement	28.9%	1.0%	1.0%	27.9%	0.9%	1.0%

Table 1: Selection efficiency and B/S rejection for some bkg sources

$e_L^- e_R^+ \rightarrow b\bar{b}$ at 500 GeV

	IDR-L	IDR-S
$Vtx+Vtx$	12.9%	12.8%
$K+K$	4.4%	4.0%
$Vtx+K$ (diff. jets)	3.9%	3.7%
$Vtx+K$ (same jet)	7.7%	7.4%

Table 2: Final selection efficiency, after double jet-charge measurement

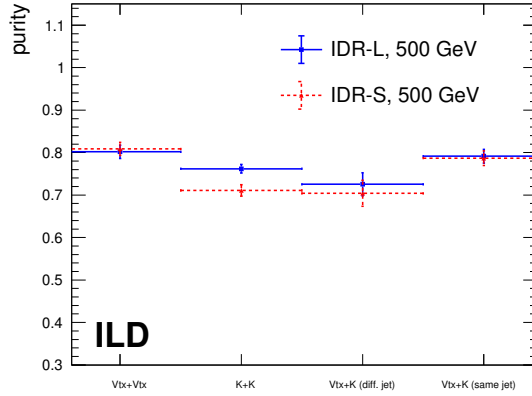


Figure 8: Purity of the methods listed in Tab. 2 used for the reconstruction of the vertex charge in the $e_L^- e_R^+ \rightarrow b\bar{b}$.

155 *4.2. Analysis details specific to the $e^+e^- \rightarrow t\bar{t}$ analysis*

156 The t quark is composed from its decay products, the b quark and the W boson and the charge of
 157 the lepton is a measure to distinguish the t from the \bar{t} quark.

158 Figure 9 shows in the left panel the energy distribution of the isolated lepton in the laboratory
 159 frame. The distribution features a maximum at around 30 GeV and a tail towards higher energies. The
 160 right panel shows the polar angle spectrum of the isolated lepton. The distribution decreases slightly
 161 with a sharp drop at the acceptance limit of the detector. The distribution reveals also acceptance
 162 drops at $\cos\theta_\ell = 0$ and $\cos\theta_\ell = 0.8$ that correspond to the position of the TPC anode plate and the
 163 barrel-endcap transition region, respectively.

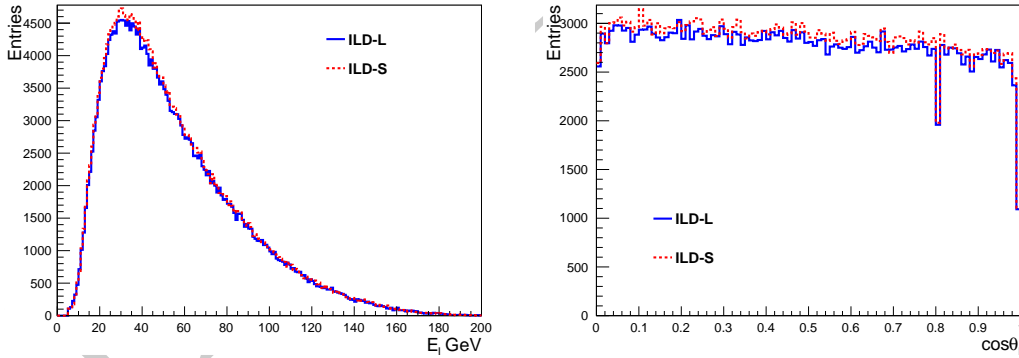


Figure 9: Left: Energy of the isolated lepton in $e_L^+ + e_R^- \rightarrow t\bar{t}$. Right: Polar angle distribution of the isolated lepton in $e_L^+ e_R^- \rightarrow t\bar{t}$.

164 For completeness Fig, 10 shows the mass distribution of the hadronic W and the hadronic t quark.

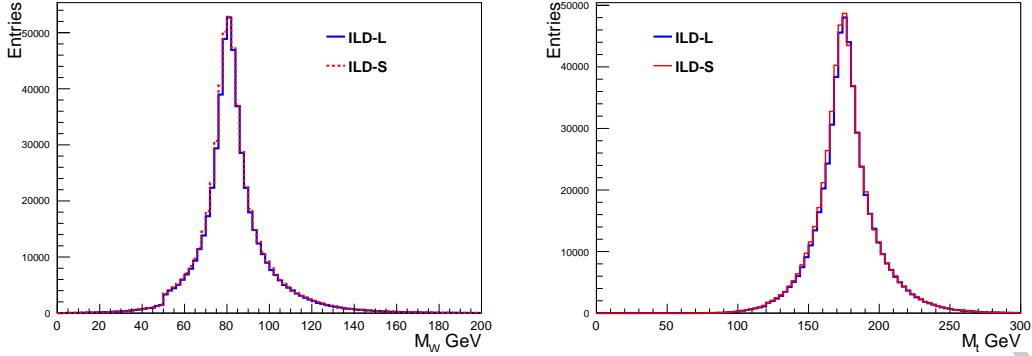


Figure 10: Left: Mass distribution of the hadronic W in $e_L^+ + e_R^- \rightarrow t\bar{t}$. Right: Mass distribution of the hadronic t quark in $e_L^+ e_R^- \rightarrow t\bar{t}$.

165 Tables 3 and 5 give the efficiencies after each cut applied for the selection of $t\bar{t}$ events. The first
 166 part lists *General selection cuts* that were already used in Ref. [5].

167 The polar angle of the t quark $\cos\theta_t$ is reconstructed from the hadronically decaying t quark. For
 168 the polar angle spectrum the charge of the t quark has to be determined and the b quark and the
 169 W -boson have to be correctly associated. This is more involved in the $e_L^- e_R^+ \rightarrow t\bar{t}$ case than in the
 170 $e_R^- e_L^+ \rightarrow t\bar{t}$ case due to the different kinematics provoked by the $V - A$ interaction of the t quark
 171 decay. The different steps for an accurate reconstruction of the polar angle spectrum are listed in the
 172 following¹.

- 173 • In a first step further cuts on the sum of the Lorentz factor of the two tops of $\gamma_t^{had} + \gamma_t^\ell > 2.4$
 174 is applied. Here γ_t^{had} is the Lorentz factor of the hadronically decaying t quark and γ_t^ℓ the
 175 Lorentz factor of the leptonically decaying t quark. In case of $e_L^- e_R^+ \rightarrow t\bar{t}$ a cut on the B -hadron
 176 momentum of $p_{B,had.} > 15$ GeV is applied in addition.
- 177 • The semi-leptonic decay of the t quark gives powerful information for the event reconstruction
 178 giving rise to the variable L_{cut} , which means the charge of the isolated lepton plus a cut on the
 179 event quality of $\chi^2 < 15$ that is motivated in Ref. [5].
- 180 • For the b quark charge determination the used methods are very much similar to those in 2. The
 181 vertex charge is supported by the requirements of $btag > 0.8$ and a minimal hadron momentum
 182 of 25 GeV as motivated in Ref. [6]².
- 183 • The various methods of measuring the b quark charge are also combined with the charge of the
 184 isolated lepton L . In this case an additional cut on $\gamma_t^{had} > 1.23$ is applied.
- 185 • The final decision on the t quark charge is obtained from the sum of the charges associated to
 186 the different methods. If the sum is smaller (greater) than zero then the hadronically decaying
 187 t quark candidate is said to be the t quark (\bar{t} quark).

188 Table 3 gives the final selection efficiency for the case $e_L^- e_R^+ \rightarrow t\bar{t}$ after the inclusion of the respective
 189 cuts. Table 4 shows the *accumulated* efficiencies for $t\bar{t}$ identification after progressive application of
 190 the various methods described in the list of items above. The addition of methods other than L_{cut}
 191 increases the efficiency by around 38%. Figure 11 shows for completeness the purity of the selection

¹We are aware that the set of cuts does not look straight forward and needs revision in the Post-IDR phase.

²In the $e^+e^- \rightarrow b\bar{b}$ analysis this additional requirement was removed. It would have to be investigated whether this requirement can be omitted in case of $e_L^- e_R^+ \rightarrow t\bar{t}$, too

$e_L^- e_R^+ \rightarrow t\bar{t}$ at 500 GeV

General selection cuts	IDR-L	IDR-S
Isolated Lepton	92.1%	92.1%
$btag_1 > 0.8$ or $btag_2 > 0.3$	81.2%	81.1%
Thrust < 0.9	81.2%	81.1%
Hadronic mass	78.2%	78.2%
Reconstructed m_W and m_t	73.4%	73.4%
t quark polar angle spectrum		
$\gamma_t^{had.} + \gamma_t^\ell > 2.4$	62.2%	61.8%
$ p_{B,had.} > 15$ GeV	34.5%	33.9%
" $t\bar{t}$ identification"	30.6%	30.2%
b quark polar angle spectrum		
No additional cuts		

Table 3: Event selection efficiencies after pre-selection and reconstruction of the polar angle spectrum of the t quark and that of the underlying b quark for the process $e_L^- e_R^+ \rightarrow t\bar{t}$.

Methods	IDR-L	IDR-S
1 L_{cut}	22.1%	21.9%
2 $L+Vtx$	28.6%	28.4%
3 $L+K$	29.6%	29.3%
4 $Vtx+Vtx$	30.1%	29.7%
5 $K+K$	30.3%	29.9%
6 $Vtx+K$ (same jet)	30.5%	30.1%
7 $Vtx+K$ (different jet)	30.6%	30.2%

Table 4: Efficiency increase after the progressive application of the various methods introduced to ensure a correct association of the W boson and the b quark in case of $e_L^- e_R^+ \rightarrow t\bar{t}$. The final efficiency in the last line of this table corresponds to the efficiency given in the line " $t\bar{t}$ identification" of Tab. 3.

192 for those cases in which the information from the t quark and the \bar{t} quark decay have been combined.
 193 As in case of $e^+e^- \rightarrow b\bar{b}$ differences between the large and the small detector are observed for those
 194 combinations that include Kaons with the biggest difference for the pure Kaon combination $K+K$.
 195 The Kaon measurement is the domain of the TPC and the two models feature different outer TPC
 196 radii.

197 As a supplementary remark please note that methods available also for the fully hadronic final
 198 state yield efficiencies of 14.4% when using Methods 4-7 of Tab. 4 and 6.9% when using only Method
 199 4, respectively.

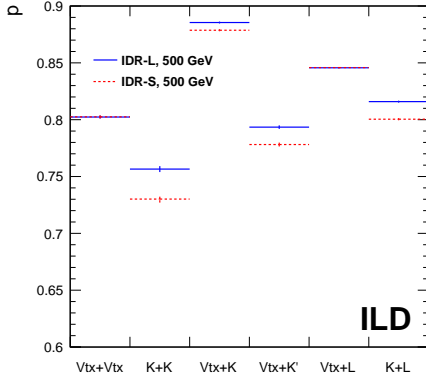


Figure 11: Purities of the various combinations to distinguish between the t and the \bar{t} quark.

 $e_R^- e_L^+ \rightarrow t\bar{t}$ at 500 GeV

General selection cuts	IDR-L	IDR-S
Isolated Lepton	94.1%	94.0%
$btag_1 > 0.8$ or $btag_2 > 0.3$	84.9%	84.8%
Thrust < 0.9	84.9%	84.8%
Hadronic mass	82.2%	82.3%
Reconstructed m_W and m_t	77.6%	77.5%
t quark polar angle spectrum		
$\gamma_t^{had.} + \gamma_t^\ell > 2.4$	64.1%	64.1%
b quark polar angle spectrum		
$Vtx+Vtx$	10.8%	10.3%

Table 5: Event selection efficiencies after pre-selection and reconstruction of the polar angle spectrum of the t quark and that of the underlying b for the process $e_R^- e_L^+ \rightarrow t\bar{t}$.

200 Table 5 shows the selection efficiencies for the case $e_R^- e_L^+ \rightarrow t\bar{t}$. The cut scenario for the reconstruction
 201 of the polar angle of the t quark is much simpler than in case of $e_L^- e_R^+ \rightarrow t\bar{t}$. The reason is that
 202 the t quark direction is in first approach given by the W boson such that a wrong association of W
 203 boson and b quark doesn't alter the t quark direction. For the polar angle spectrum of the underlying
 204 b quark the analysis is restricted to the combination of the vertex charge. This is further discussed
 205 in Sec. 5.

206 **5. Results**

207 Figure 12 shows the spectrum of the polar angle $\cos \theta_b$ after the selection given in Tabs. 1 and 2 and
 208 the application of Eq. 3 for $e_L^- e_R^+ \rightarrow b\bar{b}$. Large and small detector agree within statistical uncertainties.
 209 It seems however that there is larger migration for the small detector.

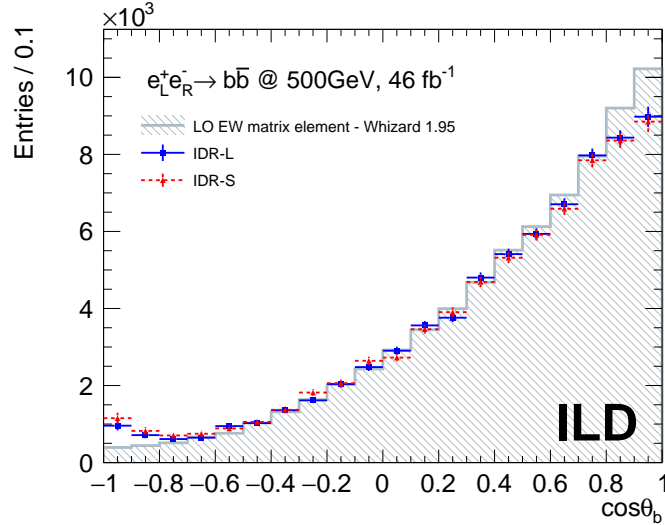


Figure 12: Polar angle spectrum for $e_L^- e_R^+ \rightarrow b\bar{b}$ at $\sqrt{s} = 500 \text{ GeV}$ after correction for acceptance and migrations due to charge mismeasurement, see Eq. 3, for the two ILD Detector models.

210 The left part of Fig. 13 shows the polar angle distribution of $t\bar{t}$ of the generated and reconstructed
 211 data for the large and the small detector models. For this all cuts and methods given in Tabs. 3
 212 and 4 have been applied. Overlaid and here and in the following figures, mainly to guide the eye,
 213 is a polynomial of second degree motivated by the approximate $d\sigma/d\cos\theta_t \sim S\cos^2\theta_t + A\cos\theta_t$
 214 dependence of the differential cross section. The right part shows the polar angle distribution of the
 215 underlying b quark for the same set of cuts. The polar spectrum can be accurately reconstructed over
 216 the entire polar angle. Acceptance drops at large absolute values of the polar angle become visible in
 217 the polar angle spectrum of the b quark (In this case no attempt was made to correct for acceptance
 218 as in Fig. 12). However, in the range $-0.8 < \cos\theta_b < 0.8$ also the polar angle of the b quark can be
 219 accurately reconstructed.

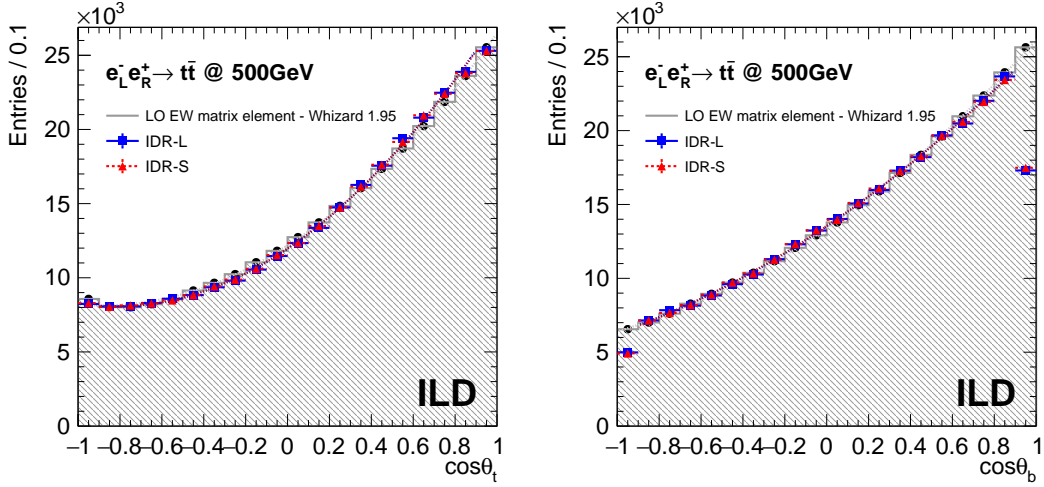


Figure 13: Results for $e_L^- e_R^+ \rightarrow t\bar{t}$ at $\sqrt{s} = 500$ GeV for the two ILD Detector models. *Left:* Polar angle distribution for t quark. *Right:* Polar angle distribution for the b quark that is issue of the t quark decay. The distributions for IDR-S is normalised to the one for IDR-L so that both histograms will be on the same level. For details on the selection, see text and Tabs. 3 and 4.

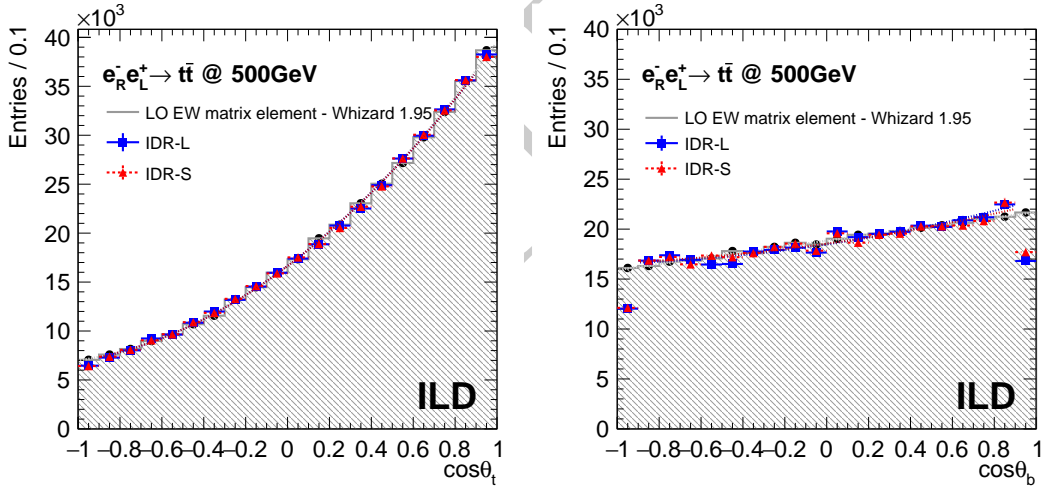


Figure 14: Same as Fig. 13 for $e_R^- e_L^+ \rightarrow t\bar{t}$. For details on the selection, see text and Tab. 5.

220 The left part of Fig. 14 shows the polar angle spectrum for the case $e_R^- e_L^+ \rightarrow t\bar{t}$ after application of
 221 the cuts introduced in Tab. 5. The generated spectrum can be very precisely reconstructed. The right
 222 hand part of Fig. 14 shows the polar angle spectrum of the underlying b quark. Here only events with
 223 consistent vertex-charge measurements have been included. The polar angle of the b quark can also
 224 in this case be very well reconstructed. However, the efficiency drops to 10% as already quantified in
 225 the lower part of Tab. 5. The inclusion of the other methods is subject to further studies. Preliminary
 226 results show that taking into account the isolated lepton “swamps” the polar angle spectrum with
 227 events in which the b quark direction is not constrained. One reason is certainly that in the case of
 228 $e_R^- e_L^+ \rightarrow t\bar{t}$ the b quark is on average softer than in the case of $e_L^- e_R^+ \rightarrow t\bar{t}$.

229 Comparing the spectra of the underlying b quarks demonstrates more clearly than the actual t quark
 230 polar angle spectra the different polarisations of the t quarks projected out by the flight direction of

231 the b quark. In case of $e_L^- e_R^+ \rightarrow t\bar{t}$ the final state is enriched with left-handed t quarks. In this case the
 232 b quark is preferably emitted in the direction of the t quark. Therefore the two polar angle spectra in
 233 Fig. 13 look similar to each other. In case of $e_R^- e_L^+ \rightarrow t\bar{t}$ the final state is enriched with right-handed
 234 t quarks. In this case the b quark is preferably emitted opposite to the direction of the t -quark. The
 235 polar angle of the b quark is a consequence of the Jacobian peak in the vicinity of $\cos\theta_{Wb} = 0$, with
 236 $\cos\theta_{Wb}$ being the opening angle between the b quark and the W boson, generated by the boost of
 237 the back-to-back configuration in the centre-of-mass frame of the decaying t quark into the laboratory
 238 frame.

239 5.1. Interpretation of the results

240 Table 6 lists the generated and reconstructed value of the forward-backward asymmetry $A_{FB, reco}^t$
 241 as an estimator for the quality of the reconstruction.

	$e_L^- e_R^+ \rightarrow t\bar{t}$		$e_R^- e_L^+ \rightarrow t\bar{t}$	
	IDR-L	IDR-S	IDR-L	IDR-S
$A_{FB, gen}^t$	0.329		0.430	
$A_{FB, reco}^t$	0.342	0.340	0.430	0.430

Table 6: Selection efficiencies and resulting $A_{FB, reco}^t$ for both beam polarisations and the two detector models under study.

242 So far the results have been presented for full beam polarisation. Using the known formula [12]

$$\sigma_{\mathcal{P}_{e^-}, \mathcal{P}_{e^+}} = \frac{1}{4} [(1 - \mathcal{P}_{e^-} \mathcal{P}_{e^+})(\sigma_{-,+} + \sigma_{+,-}) + (\mathcal{P}_{e^-} - \mathcal{P}_{e^+})(\sigma_{+,-} - \sigma_{-,+})], \quad (5)$$

243 with $\sigma_{-,+}$ and $\sigma_{+,-}$ being the fully polarised cross-sections, the results can be extrapolated to the
 244 realistic beam polarisations of $\mathcal{P}_{e^-}, \mathcal{P}_{e^+} = \mp 0.8, \pm 0.3$. The resulting Born level cross sections are
 245 1070 fb in case of $\mathcal{P}_{e^-}, \mathcal{P}_{e^+} = -0.8, +0.3$ and 519 fb in case of $\mathcal{P}_{e^-}, \mathcal{P}_{e^+} = +0.8, -0.3$. The resulting
 246 statistical errors for an integrated luminosity of $\mathcal{L} = 1600 \text{ fb}^{-1}$ at each of the two polarisation settings
 247 are given in Table 7.

	$\mathcal{P}_{e^-}, \mathcal{P}_{e^+}$	$(\delta\sigma/\sigma)_{stat.} [\%]$	$(\delta A_{FB}^t/A_{FB}^t)_{stat.} [\%]$
IDR-L	-0.8, +0.3	0.17	0.7
	+0.8, -0.3	0.25	0.53
IDR-S	-0.8, +0.3	0.17	0.7
	+0.8, -0.3	0.25	0.53

Table 7: Statistical precisions expected for the cross sections and A_{FB}^t for the case $\mathcal{P}_{e^-}, \mathcal{P}_{e^+} = -0.8, +0.3$ and the two detector models under study.

248 For both, the cross section and the forward backward asymmetry it can be expected that even at
 249 full luminosity the statistical error has to be taken into account. However, the systematic errors need
 250 to be carefully estimated. For the present analysis it would have to be checked how much the sample
 251 is contaminated by events for which the semi-leptonic decay yields τ -leptons or the τ -leptons are taken
 252 into account as in [5]. The contamination by fully hadronic $t\bar{t}$ events can be expected to be small.

253 To put the results into context, the precisions on the cross-sections and the forward-backward
 254 asymmetries are translated into precisions on electromagnetic form factors of the t quark. Figure 15
 255 shows the precisions at the 1σ level expected at ILC500. The precisions are compared with those
 256 expected after the full HL-LHC running and estimations produced for FCC-ee [13] at the same confi-
 257 dence level. For ILC500, the two sets F_1 and F_2 have been extracted separately but within each set
 258 the uncertainties have been extracted simultaneously. The projections for HL-LHC are derived from

259 the *individual* constraints of EFT Wilson coefficients presented in Tab.C2.3 of Ref. [14] (the most
 260 favorable scenario for HL-LHC). These figures demonstrate clearly the superiority of a linear e^+e^-
 261 collider with polarised beams operated at an adequate centre-of-mass energy.

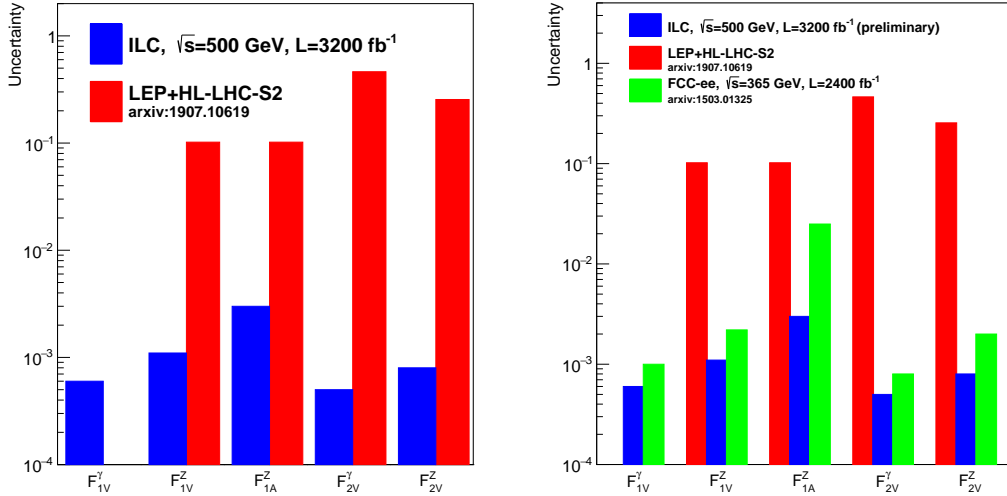


Figure 15: Precisions the on electromagnetic t quark form factors expected after ILC500 compared with those expected after the full HL-LHC running and an estimation for FCC-ee after 5000 fb^{-1} . The EFT does not include operators that map onto the F_{1V}^Y form factor. See text for further details.

262 6. Summary

263 This note presents a study of the processes $e^+e^- \rightarrow t\bar{t}$ and $e^+e^- \rightarrow b\bar{b}$ with polarised beams at
 264 $\sqrt{s} = 500$ GeV. The events are simulated and reconstructed with the large and the small models of the
 265 ILD detector.

266 In case of t quark pair production the analysis focuses on the semi-leptonic decay channel in which
 267 the isolated lepton is available for the distinction between the t quark and the \bar{t} quark. In case of
 268 the $e^+e^- \rightarrow b\bar{b}$ process the distinction has to be made by the measurement of the b quark charge,
 269 which helps also for a proper reconstruction of the $t\bar{t}$ quark pair. The charge of the b quark can be
 270 reconstructed with a purity of 80% using the combination of information available from the vertex
 271 charge, Kaons that have been measured in the TPC of ILD or isolated leptons in case of t -quark
 272 production.

273 The analysis shows that both, the large and the small detector model, are capable to provide
 274 a high precision measurement of the cross-section and the polar angle spectrum of semi-leptonic $t\bar{t}$
 275 events with a mild advantage for the large detector. Assuming a total intergrated luminosity of
 276 $\mathcal{L} = 3200 \text{ fb}^{-1}$ shared equally between the beam polarisations $\mathcal{P}_{e^-}, \mathcal{P}_{e^+} = \mp 0.8, \pm 0.3$, the cross sections
 277 of $t\bar{t}$ production can be measured to a statistical precision of about 0.2% and the forward backward
 278 asymmetry to a statistical precision of around 0.6%. The statistical precision on the cross section and
 279 the forward backward asymmetries are compatible with the scaling of the results found in [5].

280 For the first time the polar angle spectrum of the underlying b quark, issue of the t quark decay,
 281 is presented. This spectrum reveals more clearly the acceptance drop towards large polar angles. Still
 282 the polar angle of the b quark can be reconstructed accurately within $|\cos\theta| < 0.8$ for the two studied
 283 beam polarisations $\mathcal{P}_{e^-}, \mathcal{P}_{e^+} = \pm 1, \mp 1$. In case $\mathcal{P}_{e^-}, \mathcal{P}_{e^+} = +1, -1$ the efficiency drops however to
 284 10% (compared with 30% for the case $\mathcal{P}_{e^-}, \mathcal{P}_{e^+} = +1, -1$). since only the vertex charge is used for
 285 this measurement. Here further work is clearly needed to improve the event yield. Both results allow

286 however already now for the perspective that in the future the fully hadronic final state can be taken
287 into account for the analysis and that observables specific to the produced b quark can be addressed.

288 The study of the $t\bar{t}$ production has been accompanied by the second benchmark study $e^+e^- \rightarrow b\bar{b}$.
289 Since only 46 fb^{-1} are available for this channel it should be rather considered as an auxiliary study.
290 However, it is shown that the polar angle spectrum can be very well reconstructed even for the hard b
291 jets and that migrations can be controlled at a satisfactory level. It is therefore justified to conclude
292 that ILD should be able to make precision measurements in this channel even at a centre-of-mass
293 energy of 500 GeV. Although the results are similar for both the small and the large detector model,
294 this analysis, more than the analysis of the $t\bar{t}$ process reveals a slight preference for the large model.
295 This is most clearly visible in the purity of the charge measurement using Kaons, which may depend
296 on the actual TPC radius.

297 Also in the future all heavy quark studies should be carried out in close cooperation with each
298 other. As can be seen from the present study there are many common issues between the studies.
299 In the future emphasis will be put on systematic uncertainties given e.g. by hemisphere correlations.
300 These studies may be more involved in case of $t\bar{t}$ since in general the two b quarks are not back-to-back.

301 Acknowledgements

302 References

- 303 [1] F. Richard, “Present and future constraints on top EW couplings”, LAL-ORSAY-14-55, [arXiv:1403.2893](#)
304 [\[hep-ph\]](#).
- 305 [2] L. Randall and R. Sundrum, “A Large mass hierarchy from a small extra dimension”, *Phys.Rev.Lett.* **83** (1999)
306 [3370–3373](#), MIT-CTP-2860, PUPT-1860, BUHEP-99-9, [arXiv:hep-ph/9905221](#) [\[hep-ph\]](#).
- 307 [3] A. Djouadi, G. Moreau, and F. Richard, “Resolving the A(FB)**b puzzle in an extra dimensional model with an
308 extended gauge structure”, *Nucl.Phys.* **B773** (2007) 43–64, LPT-ORSAY-06-060, LAL-ORSAY-06-144,
309 [arXiv:hep-ph/0610173](#) [\[hep-ph\]](#).
- 310 [4] G. Durieux and O. Matsedonskyi, “The top-quark window on compositeness at future lepton colliders”, *JHEP* **01**
311 (2019) 072, DESY 18-114, DESY-18-114, [arXiv:1807.10273](#) [\[hep-ph\]](#).
- 312 [5] M. S. Amjad *et al.*, “A precise characterisation of the top quark electro-weak vertices at the ILC”, *Eur. Phys. J.*
313 **C75** (2015) no. 10, 512, IFIC-15-15, LAL-15-111, [arXiv:1505.06020](#) [\[hep-ex\]](#).
- 314 [6] S. Bilokin, R. Pöschl, and F. Richard, “Measurement of b quark EW couplings at ILC”, LAL-17-052,
315 [arXiv:1709.04289](#) [\[hep-ex\]](#).
- 316 [7] S. Bilokin, *Hadronic showers in a highly granular silicon-tungsten calorimeter and production of bottom and top*
317 *quarks at the ILC*. Theses, Paris Saclay, July, 2017. <https://tel.archives-ouvertes.fr/tel-01826535>.
- 318 [8] T. Behnke, J. E. Brau, P. N. Burrows, J. Fuster, M. Peskin, *et al.*, “The International Linear Collider Technical
319 Design Report - Volume 4: Detectors”, ILC-REPORT-2013-040, ANL-HEP-TR-13-20, BNL-100603-2013-IR,
320 IRFU-13-59, CERN-ATS-2013-037, COCKCROFT-13-10, CLNS-13-2085, DESY-13-062, FERMILAB-TM-2554,
321 IHEP-AC-ILC-2013-001, INFN-13-04-LNF, JAI-2013-001, JINR-E9-2013-35, JLAB-R-2013-01,
322 KEK-REPORT-2013-1, KNU-CHEP-ILC-2013-1, LLNL-TR-635539, SLAC-R-1004,
323 ILC-HIGRADE-REPORT-2013-003, [arXiv:1306.6329](#) [\[physics.ins-det\]](#). %%CITATION =
324 ARXIV:1306.6329;%%.
- 325 [9] C. Adolphsen, M. Barone, B. Barish, K. Buesser, P. Burrows, J. Carwardine, J. Clark, H. Mainaud Durand,
326 G. Dugan, E. Elsen, *et al.*, “The International Linear Collider Technical Design Report - Volume 3.II: Accelerator
327 Baseline Design”, ILC-REPORT-2013-040, ANL-HEP-TR-13-20, BNL-100603-2013-IR, IRFU-13-59,
328 CERN-ATS-2013-037, COCKCROFT-13-10, CLNS-13-2085, DESY-13-062, FERMILAB-TM-2554,
329 IHEP-AC-ILC-2013-001, INFN-13-04-LNF, JAI-2013-001, JINR-E9-2013-35, JLAB-R-2013-01,
330 KEK-REPORT-2013-1, KNU-CHEP-ILC-2013-1, LLNL-TR-635539, SLAC-R-1004,
331 ILC-HIGRADE-REPORT-2013-003, [arXiv:1306.6328](#) [\[physics.acc-ph\]](#).
- 332 [10] T. Barklow, J. Brau, K. Fujii, J. Gao, J. List, N. Walker, and K. Yokoya, “ILC Operating Scenarios”,
333 ILC-NOTE-2015-068, DESY-15-102, IHEP-AC-2015-002, KEK-PREPRINT –2015-17, SLAC-PUB-16309,
334 [arXiv:1506.07830](#) [\[hep-ex\]](#).

- 335 [11] T. Suehara and T. Tanabe, “LCFIPlus: A Framework for Jet Analysis in Linear Collider Studies”, *Nucl. Instrum.*
336 *Meth. A* **808** (2016) 109–116, [arXiv:1506.08371 \[physics.ins-det\]](#).
- 337 [12] G. Moortgat-Pick, T. Abe, G. Alexander, B. Ananthanarayan, A. Babich, *et al.*, “The Role of polarized positrons
338 and electrons in revealing fundamental interactions at the linear collider”, *Phys.Rept.* **460** (2008) 131–243,
339 CERN-PH-TH-2005-036, DCPT-04-100, DESY-05-059, FERMILAB-PUB-05-060-T, IPPP-04-50, KEK-2005-16,
340 PRL-TH-05-01, SHEP-05-03, SLAC-PUB-11087, [arXiv:hep-ph/0507011 \[hep-ph\]](#).
- 341 [13] P. Janot, “Top-quark electroweak couplings at the FCC-ee”, *JHEP* **04** (2015) 182, [arXiv:1503.01325 \[hep-ph\]](#).
- 342 [14] G. Durieux, A. Irlles, V. Miralles, A. Peñuelas, R. Pöschl, M. Perelló, and M. Vos, “The electro-weak couplings of
343 the top and bottom quarks – global fit and future prospects”, [arXiv:1907.10619 \[hep-ph\]](#).

344 A. Details on particle separation via dE/dx

345 In Fig. 8.6 of the IDR the separation power between different particle types is given. A useful
346 supplementary information of this summary is the relative frequency of the different particle types.
347 The Fig. 16 displays the normalised dE/dx spectrum for different particles in different momentum
348 ranges for the large and the small detector model. In both cases there is a clear separation of Kaons
349 from pions. The latter are however much more abundant. There is only a small population of protons.
350 Figure 17 shows the dE/dx spectra for the two processes under study.

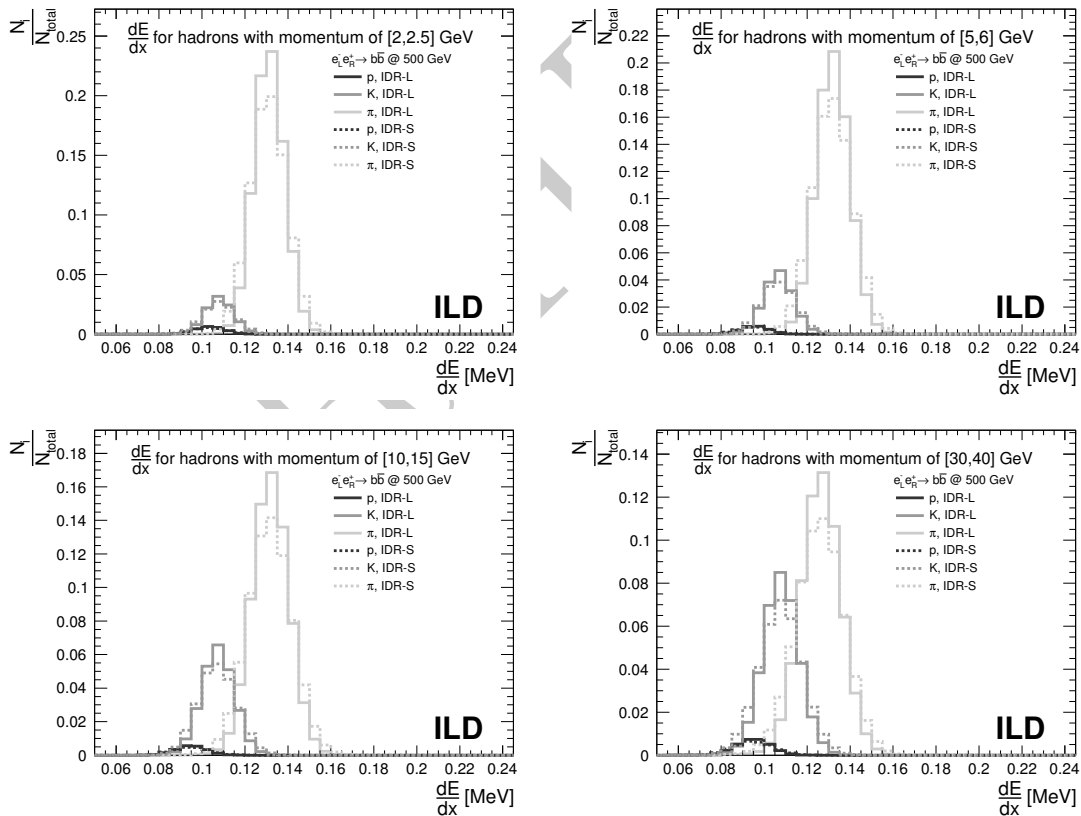


Figure 16: Projection of dE/dx for several momentum ranges. Comparison of hadron separation performance by different detector models in $b\bar{b}$ final states.

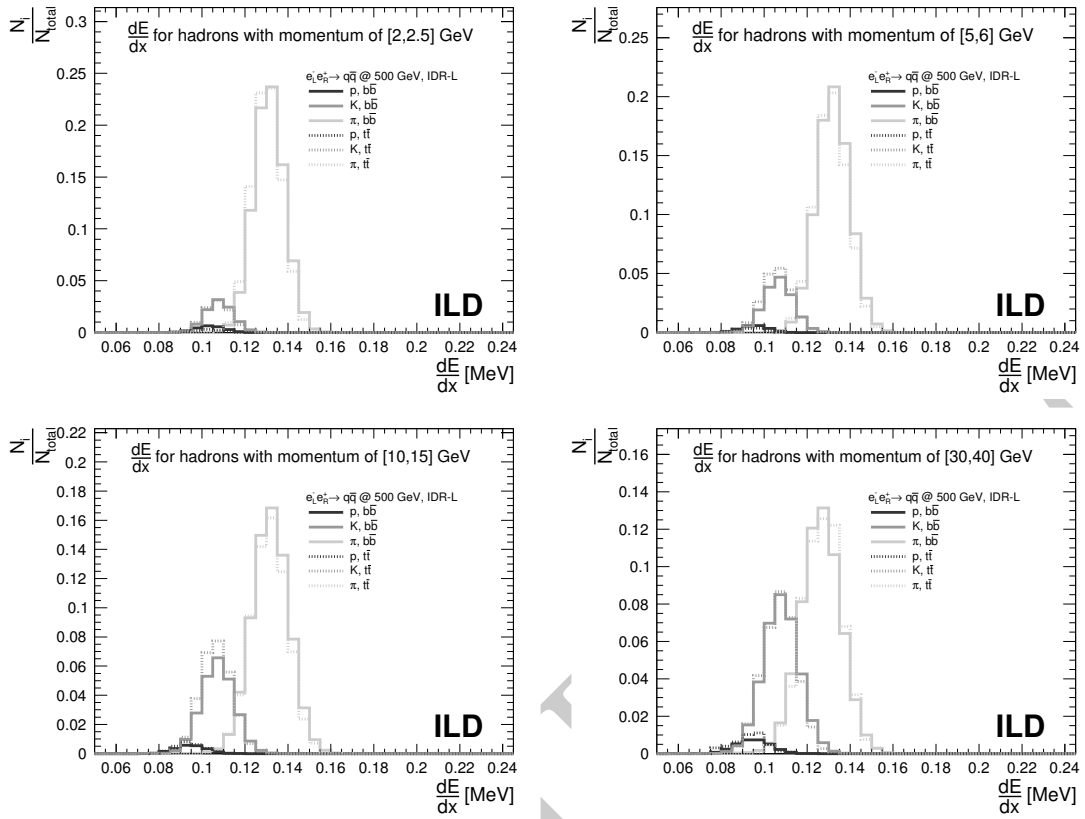


Figure 17: Projection of dE/dx for several momentum ranges. Comparison of hadron separation performance by the large model for different topologies.